

Impact of environment on dynamics of exciton complexes in a WS₂ monolayer

T. Jakubczyk,^{1,2,*} K. Nogajewski,³ M. R. Molas,³ M. Bartos,³ W. Langbein,⁴ M. Potemski,^{3,5} and J. Kasprzak^{1,2,†}

¹Univ. Grenoble Alpes, F-38000 Grenoble, France

²CNRS, Institut Néel, "Nanophysique et semiconducteurs" group, F-38000 Grenoble, France

³Laboratoire National des Champs Magnétiques Intenses,

CNRS-UGA-UPS-INS-EMFL, 25 Av. des Martyrs, 38042 Grenoble, France

⁴School of Physics and Astronomy, Cardiff University,

The Parade, Cardiff CF24 3AA, United Kingdom

⁵Faculty of Physics, University of Warsaw, ul. Pasteura 5, 02-093 Warszawa, Poland

(Dated: October 12, 2017)

Scientific curiosity to uncover original optical properties and functionalities of atomically thin semiconductors, stemming from unusual Coulomb interactions in the two-dimensional geometry and multi-valley band structure, drives the research on monolayers of transition metal dichalcogenides (TMDs). While recent works ascertained the exotic energetic schemes of exciton complexes in TMDs, we here employ four-wave mixing microscopy to indicate that their subpicosecond dynamics is determined by the surrounding disorder. Focusing on a monolayer WS₂, we observe that exciton coherence is lost primarily due to interaction with phonons and relaxation processes towards optically dark excitonic states. Notably, when temperature is low and disorder weak excitons large coherence volume results in huge oscillator strength, allowing to reach the regime of radiatively limited dephasing and we observe long valley coherence. We thus elucidate the crucial role of exciton environment in the TMDs on its dynamics and show that revealed mechanisms are ubiquitous within that family.

Introduction In spite of their illusory academic simplicity, synthetic two-dimensional (2D) materials - such as graphene, black phosphorous, and transition metal dichalcogenides (TMDs) - display stunning properties, which are also revealed in their optical responses. For instance, in monolayers (MLs) of TMDs, the reduced dielectric screening and 2D carrier confinement give rise to exotic, non-hydrogenic excitons with binding energies exceeding 0.2 eV [1], which is an asset enhancing light-matter interaction. The latter is manifested by a strong absorption and subpicosecond population lifetime, favoring formation of surface plasmon polaritons [2] and exciton-polaritons [3–5] with a valley degree of freedom - to name a few examples illustrating a technology-driven progress in the optics of TMDs. However, there is a need for an in-depth understanding of fundamental mechanisms governing exciton radiative and nonradiative recombination rates in various experimental settings. There is a large spread of reported values of exciton coherence and population decay [6] and little is known about their dependence on microscopic material properties and environmental factors, such as temperature, strain, dielectric surrounding and excitonic disorder on different length scales, generating inhomogeneous broadening σ .

The main obstacle to access these information, was a large size of the optically probed areas (typically, diameter of a few tens of micron), which are required to implement traditional approaches of nonlinear spectroscopy - such as angle-resolved four-wave mixing (FWM) - inferring decay times of populations T_1 and coherent polarizations T_2 in extended samples. We here overcome this difficulty, by exploiting phase-sensitive heterodyne

detection. The latter permits to perform FWM spectroscopy in a microscopy configuration, attaining spatial resolution of 300 nm. Using a tungsten disulphide (WS₂) ML, exhibiting the strongest optical activity among all other TMDs ML [7] we observe a giant FWM response of the resonantly generated excitons and we carry out the mapping of their dephasing time ($T_2 = 2\hbar/\gamma$), population decay time and σ . We further infer the dephasing induced by phonons, by performing FWM temperature dependence.

Additionally, two distinct types of trions (bound states of two electrons and one hole) are unambiguously identified in FWM. We show that a single electron is the ground state for optically active trions, where the additional electron and hole are within the same valley as this ground state electron (intra-valley trion), or in the opposite valley (inter-valley trion). An energetic splitting between these states due to exchange interaction was recently predicted [8], and observed [9] for WSe₂ and for WS₂ [10]. We observe the Raman quantum beats [11] resulting from this splitting, revealing coupling between both types of trions. We employ this phenomenon to measure the decay of the valley coherence T_2^{valley} [12–15], which appears to be significantly longer than previously reported.

Spectral characteristics of transitions We first perform micro-reflectance from a flake, to identify exciton (EX) and trion (TR) transitions, as shown in Fig. 1. In further experiments we employ the FWM micro-spectroscopy setup [16–18] (see *Methods*), adapted to the visible spectral range. We probe the flake with the $\mathcal{E}_{1,2,3}$ pulsed laser beams which are spectrally centered at either EX (~ 590 nm) or TR (~ 600 nm), with

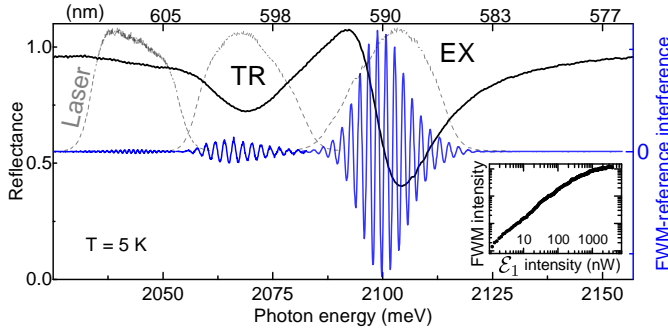


Figure 1. **Four-wave mixing micro-spectroscopy of a WS₂ monolayer.** Spectrally-resolved reflectance and FWM-reference interference at $\tau_{12} = 0.2$ ps centered at exciton (EX), trion (TR) transitions and the third (trionic) transition. The corresponding spectra of the excitation laser are given by gray dashed lines. Inset: FWM intensity dependence of EX.

a bandwidth about 7 nm (full width at half maximum, FWHM). The reference \mathcal{E}_R beam is focused on the surrounding SiO₂, so that its lineshape is not affected by a strong absorption of the flake. Fig. 1 presents the resulting FWM spectral interferograms obtained on both resonances in the WS₂ flake at T=5 K. We note that the amplitude of the TR is typically an order of magnitude weaker than the EX's one. Below the TR line we further retrieve FWM of another type of valley-trion [19]. The fringe period in Fig. 1 is given by a few pico-seconds (ps) delay between the reference pulse \mathcal{E}_R and the FWM emission. Its intensity and phase are retrieved by applying spectral interferometry. The former as a function of \mathcal{E}_1 intensity is shown in the inset, yielding the limit of the third-order $\chi^{(3)}$ regime (where further experiments are performed) up to around 100 nW. It is worth to note that FWM can be readily detected with \mathcal{E}_1 as low as 1 nW, generating a low carrier density of a few 10^8 cm⁻². At excitation stronger than 100 nW, FWM visibly starts to saturate, which we attribute to the absorption bleaching. In WS₂ MLs, the optically active exciton (EX) has a larger transition energy than the dark one [20], such that at low temperature the PL of EX is suppressed [10], as shown in the Supplementary Fig. S1. While this issue remains relevant in view of competing relaxation channels of the bright exciton, it is not an obstacle to drive its FWM: EX are resonantly and selectively created, generating a giant response, owing to the μ^4 scaling of the FWM, where μ is the oscillator strength.

Homogenous and inhomogeneous widths of the neutral exciton The EX spectral lineshape measured in reflectance (Fig. 1) is dominated by inhomogeneous broadening with a Gaussian distribution of around 15 meV FWHM. FWM spectroscopy has been conceived primarily to access the homogeneous broadening FWHM γ in an inhomogeneously broadened ensemble, exhibiting a spectral standard deviation of σ . The complex conjuga-

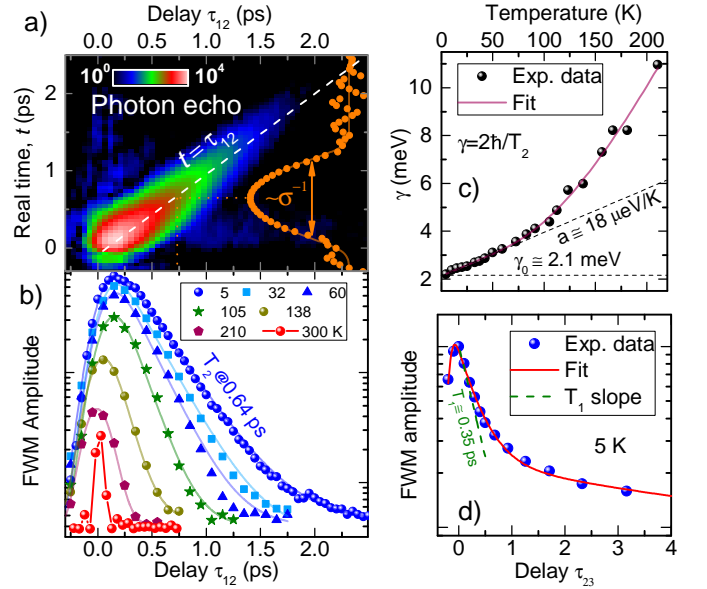


Figure 2. **Exciton dephasing in WS₂ ML measured in two-beam FWM.** a) Time-resolved FWM showing the photon echo at T= 5 K, σ is retrieved from its temporal width (orange trace). Logarithmic color scale. b) Time-integrated echo as a function of delay τ_{12} for temperatures, as indicated. The non-exponential behavior is due to a constant offset, giving a noise level. c) The retrieved homogeneous broadening versus temperature $\gamma(T)$ fitted with model described in the text, dashed lines represent parameters obtained from the fit. d) Exemplary measurement of the EX density dynamics for a given position. The initial decay T_1 is mainly due to radiative recombination T_{rad} and non-radiative relaxation T_{dark} to the EX dark state, such that $(T_1)^{-1} = (T_{rad})^{-1} + (T_{dark})^{-1}$.

te in the FWM definition, imposes phase conjugation between the first-order polarization induced by \mathcal{E}_1 and the FWM. For $\tau_{12} > \hbar/\sigma$, its transient appears as a Gaussian, known as a photon echo. It is centered at $t = \tau_{12}$ and has a FWHM, corrected with respect to the pulse duration, equal to $8 \ln(2)\hbar/\sigma$. Formation of such an echo is illustrated in Fig. 2 a, where time-resolved FWM amplitude of EX versus τ_{12} is shown. The echo develops during the initial $0 < \tau_{12} < 0.5$ ps. By inspecting FWM for later delays, for example $\tau_{12} = 0.7$ ps (orange trace) we retrieve inhomogeneous width of around 11 meV (FWHM).

Time-integrated amplitudes of the photon echo as a function of τ_{12} for different temperatures are reported in Fig. 2 b. Here, the decay reflects γ . To retrieve γ , the data are fitted with an exponential decay $\exp(-\gamma\tau_{12}/2\hbar)$, convoluted with a Gaussian to account for a pulse duration of 0.12 ps. At T=5 K we obtain $\gamma_{EX} = (2.1 \pm 0.1)$ meV, yielding dephasing time $T_2 = (620 \pm 20)$ fs. Thus EX in WS₂ shows a larger homogeneous width than its counterpart in recently investigated MoSe₂ MLs [18], in line with a superior linear absorption in WS₂ with respect to MoSe₂ [7]. The temperature dependence of γ is illustrated in Fig. 2 c. The data

are modeled [21](purple trace) with the following equation: $\gamma(T) = \gamma_0 + aT + b/[\exp(E_1/k_B T) - 1]$. The linear term [$\gamma_0 = (2.1 \pm 0.1)$ meV, $a = (0.018 \pm 0.003)$ meV/K] is attributed to low energy acoustic phonons. The latter term, with the $b = (32 \pm 6)$ meV, is attributed to thermal activation of optical phonons with dominant or mean energy $E_1 = (37 \pm 3)$ meV, which indeed supply a large density of states above $300 \text{ cm}^{-1} \simeq 37 \text{ meV}$ [22]. The phonon dephasing mechanisms are therefore similar as in MoSe₂ MLs [18] and as in semiconductor quantum wells. Above $T = 210 \text{ K}$, the FWM decay is limited by the temporal resolution, such that γ cannot be extracted, although a strong FWM is measured up to the room temperature.

Population decay A representative measurement of the population dynamics (FWM response versus τ_{23}) via three-beam FWM [17, 18] is shown in Fig. 2 d. The measurement was performed at the same spot as the dephasing study, presented in Fig. 2. The population dynamics is dominated by an initial exponential decay with a constant of $T_1 \simeq 0.35 \text{ ps}$, followed by a longer dynamics described by two additional exponential decays [23] ($T_{\text{slow}}^1 \simeq 4.7 \text{ ps}$ and $T_{\text{slow}}^2 \simeq 46 \text{ ps}$) that we can relate to phase space distribution via scattering processes and scattering back from the exciton dark ground state. We note that the portion of secondary excitons, decaying on a nano-second timescale, is at least an order of magnitude larger than on recently studied MoSe₂ MLs. This we associate with a dark exciton ground state in WS₂ and its bright character in MoSe₂ [20].

The obtained result ($T_2 \simeq 2T_1$) indicates population-limited dephasing. We attribute this fast decay to be due primarily to the fast radiative decay. Indeed, excitons in ML TMDs possess the radiative lifetime T_{rad} of a few hundred femto-seconds, as recently revealed via two-colour pump-probe [24], FWM [18, 25] and TMD polaritons studies [3–5] - all these results signify a large EX transition dipole moment and coherence volume spanning across many Bohr radii [26]. The parameter T_{dark} describing phase space distribution via scattering processes and relaxation to the dark exciton ground state is also expected to contribute to the fast initial decay. Other nonradiative recombination processes are expected to be of minor impact, as they are not faster than the decay of secondary excitons, that is $\geq 46 \text{ ps}$ (we assume that these processes have the same dynamics for both bright and dark excitons). We also note a weak role of phonons on the excitons dynamics in this low temperature range (see Fig. 2 c). To get a comprehensive view of the possible mechanisms influencing the exciton dynamics, the local insight into σ , T_2 , population decay and μ is required, and should be strengthened by imaging of these quantities across the entire flake. Crucially, such an original capability is offered by the heterodyne FWM microscopy. Thus, we now focus on the FWM mappings and analyze spatial correlations between the above parameters.

Four-wave mixing mapping In the first step, we focus on spatial variation of σ . We therefore acquire FWM spectral interferograms at $\tau_{12} = 0.6 \text{ ps}$ and retrieve time-resolved FWM amplitude of EX, while scanning over the flake surface. For each location, we inspect the width of the photon echo, from which we measure σ . The result is shown in Fig. 3 a. In the middle of the flake, we identify regions of a smaller inhomogeneous broadening, down to 10 meV, yet still largely dominating over γ . It is worth to note, that the largest σ , and thus most pronounced exciton localization, is measured at the borders of the flake. This is related to the strain gradients and variations of the dielectric screening by the substrate, which are expected to be strong along the edges. These locations are preferential for wrinkling, local deformations and lattice defects creating deep potential centers trapping individual emitters (see supplementary Fig. S1 d). As an origin of σ , we point toward a local strain and charges trapped on a flake. We note that suspended ML flakes displayed comparable σ (see supplementary Fig. S3), excluding the interface roughness between the SiO₂ and the flake as a principal source of inhomogeneity. Newly, it has been found that σ is reduced by encapsulating a flake in hexagonal boron nitride [27, 28]: FWM performed on such heterostructure indeed has revealed reduction of σ , however its complete cancelation has not been observed (not shown). Moreover, a reduced spectral jitter was observed on non-insulating substrates [29], helping to get rid of trapped charges, further indicating decisive role of charge fluctuation on the inhomogeneous broadening.

In the next step, we focus on the area exhibiting a large variation of σ , marked with a square in Fig. 3 a. Again we perform mappings, this time varying also the delay τ_{12} for each position. Such retrieved T_2 and σ are presented as color-coded maps in Fig. 3 b and c, respectively. Their spatial correlation is striking and emphasized in Fig. 3 d: the fastest dephasing is measured at the areas of smallest σ . We interpret this as follows. Center of mass of two-dimensional excitons moves within a disordered potential landscape [30], arising from the variation dielectric contrasts, strain from the substrate, uncontrollable impurities, vacancies, etc. Through the Schrödinger equation, the disorder acts on the wave-function localization in real space and thus results in its delocalization in k-space, modifying radiative rates with respect to free excitons. In other words, the disorder mixes the states inside and outside of the radiative cone, and thus creates a distribution of states with an oscillator strength reduced as compared to ones fully in the radiative cone, and spread in energy, adding up to σ . Note, that this localization is weak [31] comparing to localization resulting from deep traps [32], resulting in a distinctive emission band well below the EX emission (see Supplementary Information Fig. S1 d). As presented in Fig. 3 d, T_2 starts to decrease only for a sufficiently low σ , where the ra-

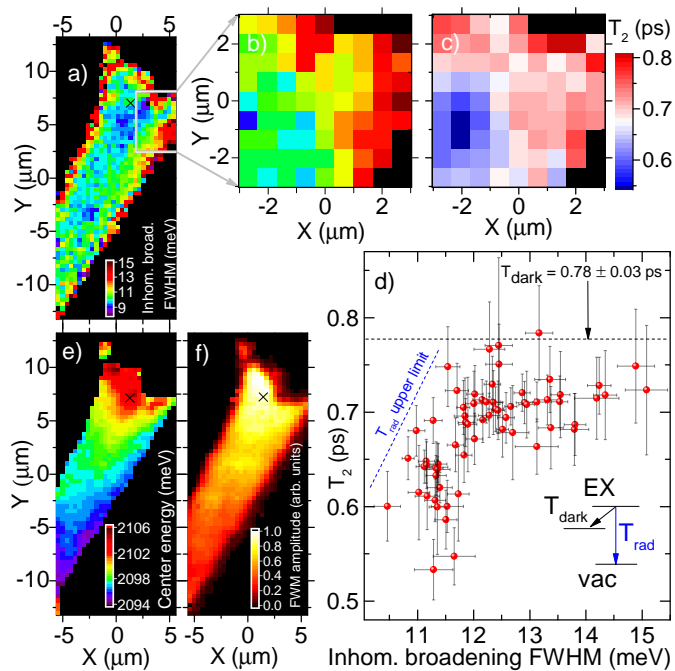


Figure 3. **Spatially-resolved probing of EX coherence in a WS₂ ML via FWM hyperspectral imaging.** a) Spatial imaging of the inhomogeneous broadening σ retrieved from time-resolved FWM at $\tau_{12} = 0.6$ ps. b) Zoomed map of inhomogeneous broadening and (c) dephasing time. d) Correlation between homogeneous and inhomogeneous broadenings, indicating radiative rate governed by localization via disorder and illustrating competition between radiative recombination and non-radiative EX shuffling to its dark state (sketched). The dashed black line indicates T_{dark} extracted from a fit (see the Supporting Information). e) Hyperspectral FWM imaging, $\tau_{12} = 0.2$ ps, hue indicates transition energy. f) Time-integrated FWM amplitude reflecting μ , linear scale over an order of magnitude. The black cross indicates location where results presented on Figs. 2 and 4 were obtained.

diative decay time T_{rad} becomes fast enough to compete with another channel, identified as the EX relaxation to the dark ground state. Such channel was not observed in MoSe₂ displaying a bright exciton ground state (see Supplementary Fig. S3a) and MoS₂ (not shown). Conversely, for largest σ , the non-radiative decay dominates, as the T_{rad} is increased through the localization. These spatial correlations demonstrate that radiative rates and dephasing of excitons in ML of TMDs are governed by exciton localization imposed by a local disorder.

The slope of the transition energy owing to the strain gradient is observed in Fig. 3e, where the center transition energy is encoded in a hue level. In Fig. 3f we present time-integrated FWM amplitude of the EX transition (corrected by the excitation lineshape) reflecting μ . Comparing Fig. 3f with Fig. 3a, we note that the areas of the smallest σ yield the strongest FWM (see also Supplementary Fig. 3). This is because with decreasing σ

(disorder), the spatial overlap between excitons increases, enhancing the EX interaction strength and thus resulting in a more intense time-integrated FWM. We note that the largest oscillator strength is observed in areas with the lowest transition energy.

Valley-trion structure We now turn to investigation of the trion transition (TR) [10]. The latter is formed when an additional electron occupies the lowest conduction band, as depicted in the inset of Fig. 4a. Depending on its spin, one can form a singlet state (intra-valley trion, intra-TR) or a triplet-state (inter-valley trion, inter-TR) [10, 33]. To address coherence dynamics of these TR, $\mathcal{E}_{1,2,3}$ are prepared co-circularly, selectively addressing K+ valleys. We investigate it at the same spatial location as for experiments illustrated on Fig. 2, yielding low σ and marked with a cross on Fig. 4a, e and f. Similarly as for EX, we obtain a single exponential decay yielding the averaged TR dephasing $T_2(\text{TR}) = (440 \pm 10)$ fs. This faster dephasing with respect to EX is attributed to fast TR relaxation into the lower lying dark states, leaving an electron with a varying momentum, and inducing additional dephasing via final state damping.

When $\mathcal{E}_{1,2,3}$ are co-linear, K+ and K- valleys are equally excited, as linearly polarized light contains both circularly polarized components. As a result, intra-TR and inter-TR transitions are activated in both valleys. In particular, intra-TR in K+ and inter-TR in K- valley share the same ground state (corresponding to the presence of an electron in the lowest conduction band, labeled with a yellow arrow in the inset in Fig. 4a), forming a coupled V-type system. In such a configuration, \mathcal{E}_1 and \mathcal{E}_2 generate valley coherence between both types of trions resulting in the Raman quantum beats [11], as sketched in the inset in Fig. 4a. Owing to the TR singlet-triplet splitting [10], labeled as Δ_{ST} , the phase of this coherence evolves when increasing τ_{12} . Therefore, the measured coherence dynamics, shown in Fig. 4a, displays beating [11] with a period $T_{\text{ST}} \simeq 0.71$ ps, yielding $\Delta_{\text{ST}} = 2\pi\hbar/T_{\text{ST}} = 5.8$ meV.

To measure the TR density dynamics we perform the τ_{23} -dependence of the FWM [18] for a fixed $\tau_{12} = 0.2$ ps. Once again, via co-circular excitation we selectively probe the intra-TR dynamics. As presented in Fig. 4b, it displays a fast monotonous decay, owing to the relaxation into the dark exciton state, followed by a slower revival of the FWM generated by the dark excitons relaxing back into the light cone [18]. This interpretation is strengthened by comparing the TR dynamics in WS₂ with the one measured in MoSe₂ ML (see Supplementary Fig. S4), exhibiting optically bright ground state. In the latter case, as the TR recombination leaves an electron with a varying momentum and relaxation to lower energy state is not possible, we observe a substantially longer TR radiative decay with respect to EX.

It is worth pointing out that no FWM is observed (ei-

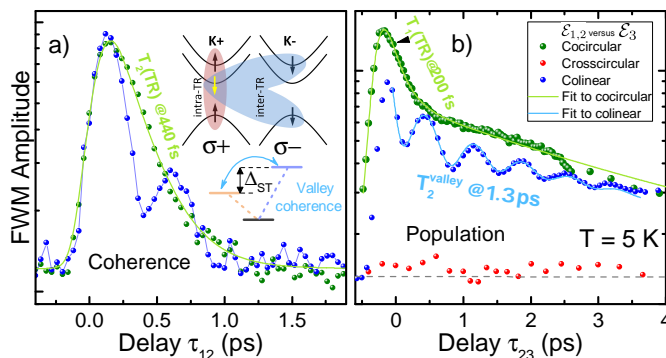


Figure 4. **FWM of the intra- and inter-valley trions in a WS₂ ML.** a) Trion coherence dynamics measured in co-circular (brown) and co-linear (green) polarizations of $\mathcal{E}_{1,2,3}$. Inset: Intra-TR in K+ valley and inter-TR in K- valley are Raman-coupled by sharing the same ground state (yellow electron, symbolized with a down-arrow). b) Population dynamics measured in co-circular and co-linear polarizations of $\mathcal{E}_{1,2,3}$. Semi-transparent traces are the fitted dynamics. Owing to σ , the measured contrast of oscillations is less than simulated. For the cross-circular setting of $\mathcal{E}_{1,2}$ and \mathcal{E}_3 the measured FWM is at the noise level (gray dashed line), indicating a strongly suppressed inter-valley scattering.

ther at TR or EX) for opposite circular polarizations of $\mathcal{E}_{1,2}$ and \mathcal{E}_3 pointing towards a robust valley polarization in WS₂ MLs.

Upon co-linear excitation, the initial density dynamics displays again an oscillatory behavior: the first two pulses do not only create the intra-TR and inter-TR populations, but also induce the valley coherence between them, once more generating the Raman quantum beats [11]. All these ingredients contribute to the FWM signals, which we model with a phenomenological fitting curve (see Supporting Information) and extract the valley coherence dephasing time of $T_2^{\text{valley}} = (1.3 \pm 0.2)$ ps. Such a record value, much longer than previously reported [12–15] and measured on location with low σ confirms recent reports suggesting that a shallow disorder potential plays a critical role in the exciton valley coherence [34]. For longer delays the valley coherence has dephased, such that the subsequent exciton dynamics is similar for both polarization configuration. Thus both TR transitions of WS₂ are here unveiled via FWM, whereas they cannot be distinguished in reflectance owing to the spectral splitting smeared out by σ_{TR} . Similar values of Δ_{ST} were retrieved when varying the position on the flake.

To conclude, we demonstrated a giant nonlinear optical response of exciton complexes in WS₂ MLs. The substantial enhancement of the FWM retrieval efficiency with respect to standard semiconductor quantum wells, was exploited to unravel the impact of a local disorder in two-dimensional systems onto exciton dynamics and dephasing. The valley degree of freedom was unveiled, when considering the trion structure. Our results indicate that

coherent nonlinear microscopy is suited to explore optical properties of emerging optoelectronic and optomechanical [35] devices and heterostructures [27] made of layered semiconductors. An alluring perspective is to image the exciton coherent dynamics on a nanometer areas and to conjugate it with the structural properties of TMDs, which can be revealed down to atomic scale using scanning tunneling microscopy. This could be achieved by transferring our methodology towards the nanoscopic regime [36, 37], offering a spatial resolution of a few tens of nanometers.

ACKNOWLEDGEMENT

We acknowledge the financial support by the European Research Council (ERC) Starting Grant PICSEN (grant no. 306387), the ERC Advanced Grant MOMB (grant no. 320590), the EC Graphene Flagship project (No. 604391) and the ATOMOPTO project within the TEAM programme of the Foundation for Polish Science co-financed by the EU within the ERDFund. We also acknowledge the technical support from Nanofab facility of the Institute Néel, CNRS UGA.

METHODS

We employ an optical parametric oscillator (Inspire 50 by Radiantis pumped by Tsunami Femto by Spectra-Physics) to create a triplet of short laser pulses around 600 nm: \mathcal{E}_1 , \mathcal{E}_2 and \mathcal{E}_3 , with adjustable delays τ_{12} and τ_{23} , as depicted in the Supplementary Fig. S1. The three beams are injected co-linearly into the microscope objective (Olympus VIS, NA=0.6), installed on a XYZ piezo stage. They are focused down to the diffraction limit of $0.6 \mu\text{m}$, onto the sample placed in a helium-flow cryostat. $\mathcal{E}_{1,2,3}$ are pre-chirped by using a geometrical pulse shaping [17], so as to attain close to Fourier-limited, 120 fs pulses on the sample. The WS₂ ML flake was mechanically exfoliated from a bulk crystal purchased from HQ-graphene and deposited on a 90 nm thick SiO₂ substrate.

The FWM generated within the sub-wavelength (approximately half of the waist) area, diffracts in all directions. There is therefore no k-vector matching condition, on which most FWM experiments rely on. Instead, our microscopy approach imposes the signal to be selected in phase, by performing optical heterodyning. By employing acousto-optic deflectors operating at different radio-frequencies $\Omega_{1,2,3}$, the phases within the pulse trains $\mathcal{E}_{1,2,3}$ are modulated by $n\Omega_{1,2,3}/\nu$, where ν and n denote the laser repetition rate and pulse index within the train, respectively. As a result, the FWM polarization - which in the lowest, third-order is proportional to $\mu^4 \mathcal{E}_1^* \mathcal{E}_2 \mathcal{E}_3$ - evolves with the phase $n(\Omega_3 + \Omega_2 - \Omega_1)/\nu$. This specific phase-drift is locked onto the reference pulse

\mathcal{E}_R , overlaid with the reflected light, and thus producing a stationary interference with the FWM field. The background free interference [16] is spectrally dispersed by an imaging spectrometer and detected on a CCD camera.

* tomasz.jakubczyk@neel.cnrs.fr

† jacek.kasprzak@neel.cnrs.fr

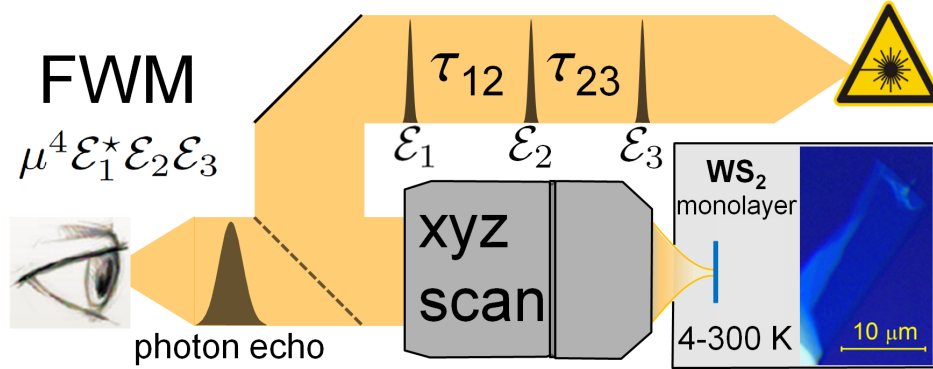
- [1] Chernikov, A. *et al.* Exciton binding energy and nonhydrogenic Rydberg series in monolayer WS₂. *Phys. Rev. Lett.* **113**, 076802 (2014).
- [2] Zhou, Y. *et al.* Probing dark excitons in atomically thin semiconductors via near-field coupling to surface plasmon polaritons. *arXive* (2017).
- [3] Liu, X. *et al.* Strong light-matter coupling in two-dimensional atomic crystals. *Nat. Phot.* **9**, 30 (2014).
- [4] Dufferwiel, S. *et al.* Exciton-polaritons in van der Waals heterostructures embedded in tunable microcavities. *Nat. Commun.* **6**, 8579 (2015).
- [5] Lundt, N. *et al.* Room-temperature Tamm-plasmon exciton-polaritons with a WSe₂ monolayer. *Nat. Commun.* **7**, 13328 (2016).
- [6] Moody, G., Schaibley, J. & Xu, X. Exciton dynamics in monolayer transition metal dichalcogenides. *JOSA B* **33**, C39–C49 (2016).
- [7] Li, Y. *et al.* Measurement of the optical dielectric function of monolayer transition-metal dichalcogenides: MoS₂, MoSe₂, WS₂, and WSe₂. *Phys. Rev. B* **90**, 205422 (2014).
- [8] Yu, H., Liu, G.-B., Gong, P., Xu, X. & Yao, W. Dirac cones and dirac saddle points of bright excitons in monolayer transition metal dichalcogenides. *Nature communications* **5**, 3876 (2014).
- [9] Jones, A. M. *et al.* Excitonic luminescence upconversion in a two-dimensional semiconductor. *Nat. Phys.* **12**, 323–327 (2016).
- [10] Plechinger, G. *et al.* Trion fine structure and coupled spin-valley dynamics in monolayer tungsten disulfide. *Nat. Comm.* **7**, 12715 (2016).
- [11] Ferrio, K. B. & Steel, D. G. Raman quantum beats of interacting excitons. *Phys. Rev. Lett.* **80**, 786 (1998).
- [12] Jones, A. M. *et al.* Optical generation of excitonic valley coherence in monolayer wse₂. *Nature nanotechnology* **8**, 634–638 (2013).
- [13] Hao, K. *et al.* Direct measurement of exciton valley coherence in monolayer WSe₂. *Nat. Phys.* **12**, 677–682 (2016).
- [14] Hao, K. *et al.* Trion valley coherence in monolayer semiconductors. *2D Materials* **4**, 025105 (2017).
- [15] Ye, Z., Sun, D. & Heinz, T. F. Optical manipulation of valley pseudospin. *Nature physics* **13**, 26–29 (2017).
- [16] Langbein, W. & Patton, B. Heterodyne spectral interferometry for multidimensional nonlinear spectroscopy of individual quantum systems. *Opt. Lett.* **31**, 1151 (2006).
- [17] Fras, F. *et al.* Multi-wave coherent control of a solid state single emitter. *Nat. Phot.* **10**, 155 (2016).
- [18] Jakubczyk, T. *et al.* Radiatively limited dephasing and exciton dynamics in MoSe₂ monolayers revealed with four-wave mixing microscopy. *Nano Lett.* **16**, 5333 (2016).
- [19] Molas, M. R. *et al.* Optical response of monolayer, few-layer and bulk tungsten disulfide. *Nanoscale* – (2017).
- [20] Molas, M. R. *et al.* Brightening of dark excitons in monolayers of semiconducting transition metal dichalcogenides. *2D Materials* **4**, 021003 (2017).
- [21] Rudin, S., Reinecke, T. & Segall, B. Temperature-dependent exciton linewidths in semiconductors. *Phys. Rev. B* **42**, 11218 (1990).
- [22] Molina-Sánchez, A. & Wirtz, L. Phonons in single-layer and few-layer MoS₂ and WS₂. *Phys. Rev. B* **84**, 155413 (2011).
- [23] Scarpelli, L. *et al.* Resonantly excited exciton dynamics in two-dimensional MoSe₂ monolayers. *Phys. Rev. B* **96**, 045407 (2017).
- [24] Poellmann, C. *et al.* Resonant internal quantum transitions and femtosecond radiative decay of excitons in monolayer WSe₂. *Nat. Mater.* **14**, 889 (2015).
- [25] Moody, G. *et al.* Intrinsic homogeneous linewidth and broadening mechanisms of excitons in monolayer transition metal dichalcogenides. *Nat. Commun.* **7**, 8315 (2015).
- [26] Feldmann, J. *et al.* Linewidth dependence of radiative exciton lifetimes in quantum wells. *Phys. Rev. Lett.* **59**, 2337 (1987).
- [27] Cadiz, F. *et al.* Excitonic linewidth approaching the homogeneous limit in MoS₂ based van der Waals heterostructures: accessing spin-valley dynamics. *Phys. Rev. X* **7**, 021026 (2017).
- [28] Ajayi, O. A. *et al.* Approaching the intrinsic photoluminescence linewidth in transition metal dichalcogenide monolayers. *2D Mater.* **4**, 031011 (2017).
- [29] Iff, O. *et al.* Substrate engineering for high-quality emission of free and localized excitons from atomic monolayers in hybrid architectures. *Optica* **4**, 669–673 (2017).
- [30] Savona, V. & Langbein, W. Realistic heterointerface model for excitonic states in growth-interrupted GaAs quantum wells. *Phys. Rev. B* **74**, 75311 (2006).
- [31] Singh, A. *et al.* Trion formation dynamics in monolayer transition metal dichalcogenides. *Physical Review B* **93**, 041401 (2016).
- [32] Hichri, A., Ben Amara, I., Ayari, S. & Jaziri, S. Exciton center-of-mass localization and dielectric environment effect in monolayer WS₂. *Journal of Applied Physics* **121**, 235702 (2017).
- [33] Singh, A. *et al.* Long-lived valley polarization of intravalley trions in monolayer WSe₂. *Phys. Rev. Lett.* **117**, 257402 (2016).
- [34] Tran, K. *et al.* Disorder-dependent valley properties in monolayer WSe₂. *Phys. Rev. B* **96**, 041302 (2017).
- [35] Morell, N. *et al.* High quality factor mechanical resonators based on WSe₂ monolayers. *Nano Lett.* **16**, 5102 (2016).
- [36] Aeschlimann, M. *et al.* Coherent two-dimensional nanoscopy. *Science* **333**, 17231726 (2011).
- [37] Kravtsov, V., Ulbricht, R., Atkin, J. M. & Raschke, M. B. Plasmonic nanofocused four-wave mixing for femtosecond near-field imaging. *Nat. Nanotech.* **11**, 459 (2015).

SUPPLEMENTARY MATERIAL

Impact of environment on dynamics of exciton complexes in a WS₂ monolayer

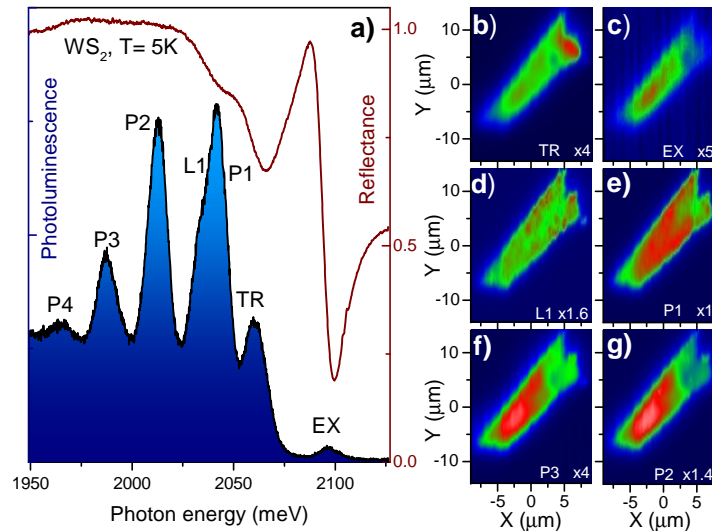
T. Jakubczyk, K. Nogajewski, M. R. Molas, M. Bartos, W. Langbein, M. Potemski, and J. Kasprzak

RATIONALE OF THE EXPERIMENT



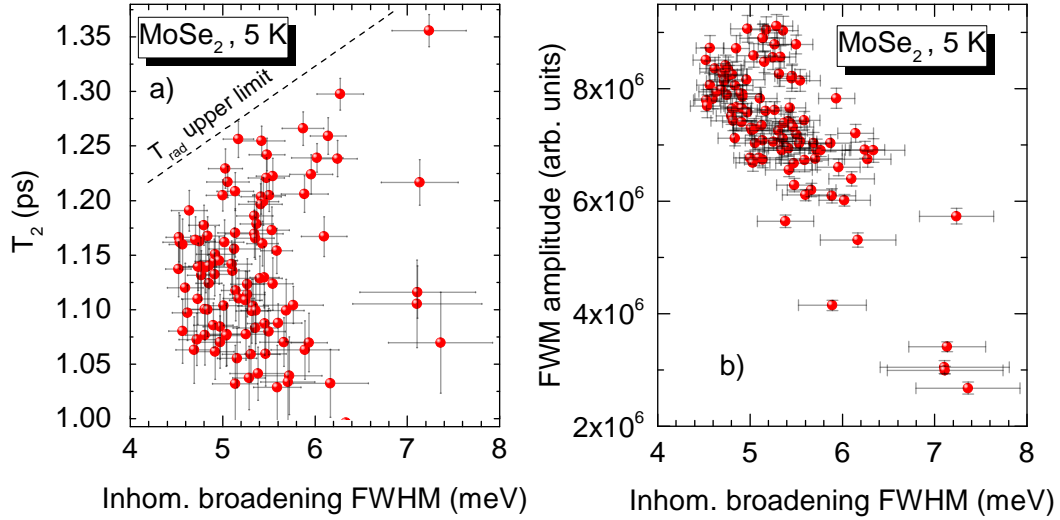
Supplementary Figure S1. Cartoon illustrating rationale of the experiment. The upper-right pictograph represent the used laser chain (CW 532 nm → Ti:Sapphire, femto-second 810 nm → OPO, femto-second pulses in VIS range). The lower-left pictograph (an eye) symbolizes the detection via heterodyne spectral interferometry approach [16].

PHOTOLUMINESCENCE HYPERSPECTRAL IMAGING

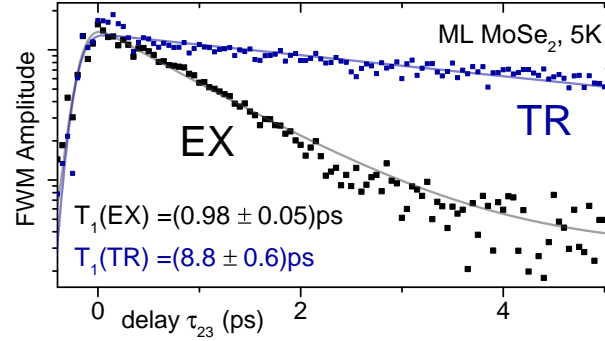


Supplementary Figure S2. **Photoluminescence hyperspectral imaging of a WS₂ monolayer at T= 5K.** a) As the optically active exciton (EX) is an excited state, its PL is strongly quenched. TR labels the negative trion. P1 was recently interpreted as another type of valley-trion [19] coinciding with the dark EX. The origin of peaks P2, P3 and P4 remains unexplained. The reflectance is given in red, for comparison with the PL. The spatial imaging spectrally integrated across the peaks, as indicated, is shown in (b-g). L1 indicates spectrally narrow, strongly localized states, which are formed at the low energy side of P1. CW excitation at 450 nm with $\simeq 5 \mu\text{W}$ at the sample.

COMPLEMENTARY RESULTS OBTAINED ON MoSe₂ MONOLAYERS



Supplementary Figure S3. **Measurements at MoSe₂ monolayer presented in Ref. [18]** a) Correlation between homogeneous and inhomogeneous broadenings, indicating radiative rate governed by localization via disorder. Note that comparing to WS₂ no saturation is observed for large inhomogeneous broadening values. We interpret the vertical spread of experimental values as resulting from activation of non-radiative recombination and fast scattering out of radiative cone, resulting in faster decoherence. Therefore, for each value of inhomogeneous broadening, only the upper point correspond to radiatively limited dephasing. b) Time-integrated FWM amplitude versus inhomogeneous broadening, the areas of the smallest σ yield the strongest FWM. This is because with decreasing σ (disorder), the spatial overlap between excitons increases, enhancing the EX interaction strength and thus resulting in a more intense time-integrated FWM response.



Supplementary Figure S4. **Density dynamics measured at EX and TR in a MoSe₂ monolayer, hosting optically bright exciton in the ground state.** The TR lifetime is an order of magnitude longer than the EX one.

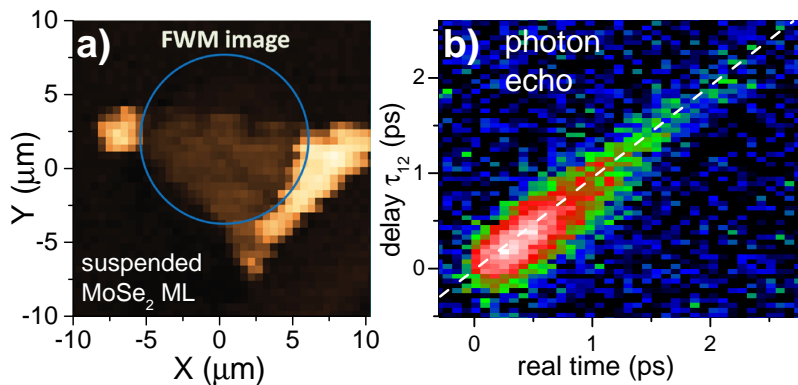
MAPPING OF THE EXCITON POPULATION DYNAMICS IN WS₂ EMPLOYING SPATIALLY-RESOLVED THREE-BEAM FWM

EXTRACTING OF T_{dark} FROM THE T_2 VS. INHOMOGENEOUS BROADENING DEPENDENCE

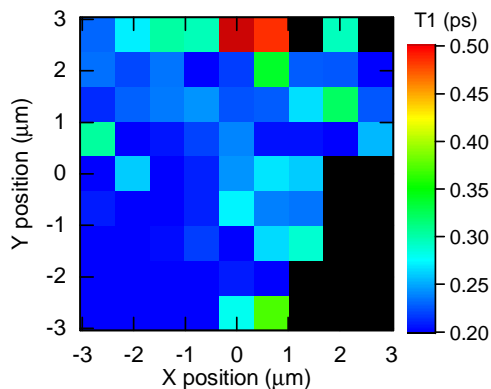
To extract T_{dark} we fit the following phenomenological dependence to data presented on Fig. 3 d:

$$1/T_2 = (A\sigma + B) + \frac{1}{T_{dark}} \quad (1)$$

and obtain $T_{dark} = 0.78 \pm 0.03 \text{ ps}$.



Supplementary Figure S5. **FWM micro-spectroscopy of a suspended MoSe₂ monolayer flake.** a) Time-integrated FWM imaging of the flake exfoliated onto a hole-aperture (indicated with a blue circle), surrounded by a SiO₂ substrate. A weakened FWM response is due to a lower laser field intensity at the aperture with respect to the substrate. b) An exemplary photon echo, measured via two-beam FWM, at the suspended part of the flake. Similar traces were obtained on other locations, both at the suspended and non-suspended parts. This indicated that the contact with the substrate is not the culprit of the inhomogeneous broadening.



Supplementary Figure S6. **Mapping of T_1 (the fastest decay component) performed on the same location as maps on Fig. 3 b and c.** Crucially, the areas characterized by a fastest T_1 also display short T_2 and the smallest σ (compare to Fig. 3 a, b and c).

RAMAN COHERENCE FIT

We fit the FWM amplitude vs τ_{23} dependence measured in colinear configuration on the TR, which is presented on Fig. 4 b, with a phenomenological model of the following form:

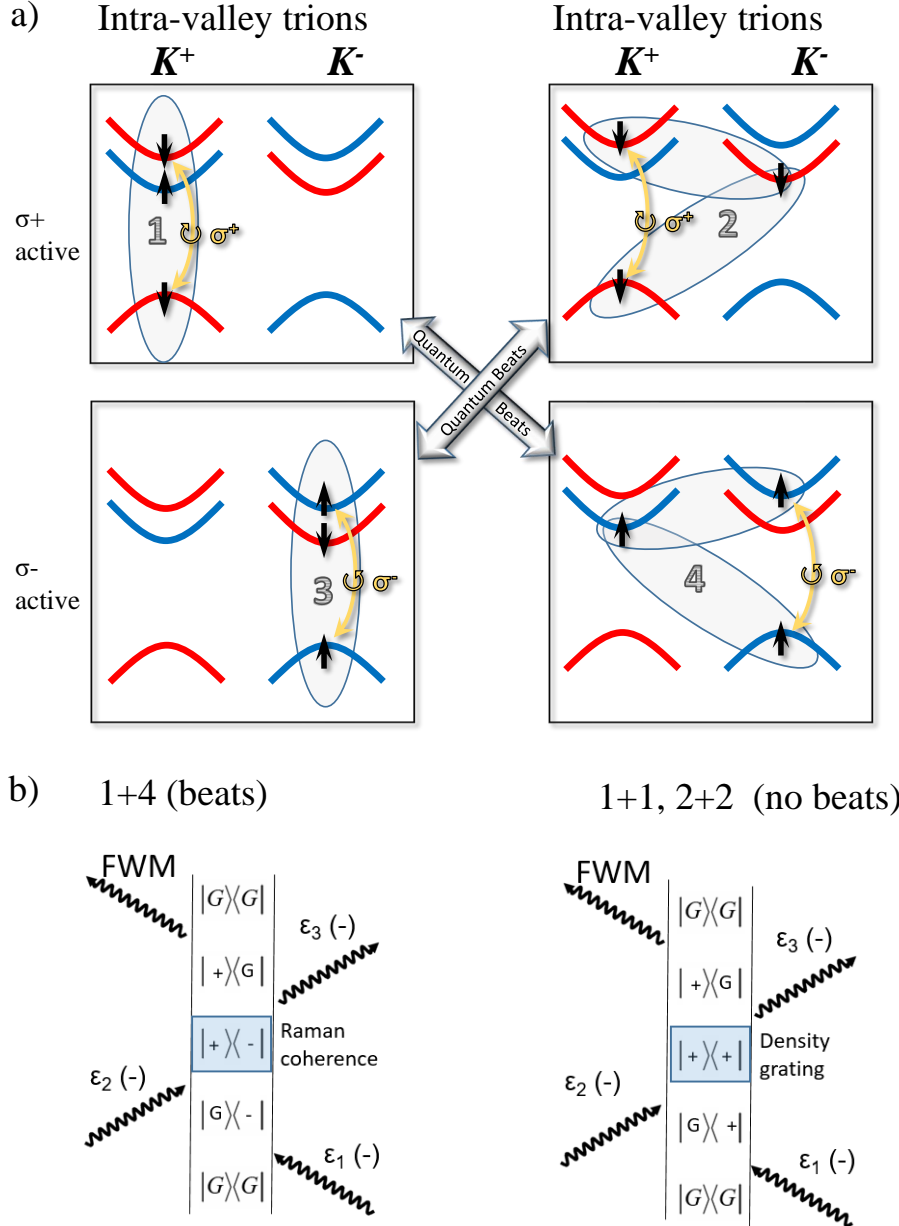
$$y_0 + \left(A e^{-\frac{\tau_{23}}{T_{\text{fast}}}} + B e^{-\frac{\tau_{23}}{T_{\text{slow}}}} \right) \left(e^{-\frac{\tau_{23}}{T_2^{\text{valley}}}} \cos \left(\frac{\Delta_{ST}}{\hbar} \tau_{23} + \phi \right) + 2 \right), \quad (2)$$

where T_2^{valley} is the valley coherence decay constant, T_{fast} and T_{slow} describe the fast and slow population decay components, respectively, while A and B are their amplitudes, y_0 is the background signal and Δ_{ST} is the TR singlet-triplet splitting. Table I presents the obtained fitting parameters. We performed fits on data obtained on different spots and values presented without experimental error here were typical values obtained from those fits. Therefore, only three free fitting parameters were used to fit data presented in the article (A , B and T_2^{valley}).

TABLE I. Raman coherence fit results

A	B	Δ_{ST} [meV]	T_{fast} [ps]	T_{slow} [ps]	T_2^{valley} [ps]	y_0
6547 ± 313	2247 ± 15	5.76	0.2	4	1.33 ± 0.07	1220

TRION TRANSITION - FEYNMAN DIAGRAM OF POSSIBLE QUANTUM PATHWAYS



Supplementary Figure S7. Scheme of possible trion electronic configurations and Feynman diagrams of possible quantum pathways under colinear excitation (we omit the symmetric diagrams, which can be obtained by inverting valleys and polarizations to opposite).